Quantitative rescattering theory of correlated two-electron momentum spectra for strong-field nonsequential double ionization of helium

Zhangjin Chen,[1] Yaqiu Liang,[1,2] and C. D. Lin[1]

[1]*J. R. Macdonald Laboratory, Physics Department, Kansas State University, Manhattan, Kansas 66506-2604, USA*
[2]*College of Physics, Liaoning University, Shenyang 110036, People's Republic of China*

We study the correlated two-electron momentum spectra of the nonsequential double ionization (NSDI) of an atom in an intense laser field based on the recently developed quantitative rescattering (QRS) theory. According to the rescattering model, an electron that was released earlier in the laser pulse may return to collide again with the target ion. NSDI can occur directly if this electron knocks out another electron in a process similar to the $(e,2e)$ process or indirectly by first exciting the target ion to an excited state which is later ionized by the laser field. Using QRS, we obtain the returning electron wave packet. By multiplying this wave packet with standard field-free $(e,2e)$ differential cross sections, or with inelastic electron-impact excitation cross sections and the subsequent tunneling ionization, we obtain the correlated two-electron momentum spectra. The calculated spectra agree mostly with the experimental data. However, experimental data show additional features that cannot be accounted for by these two mechanisms only, and other mechanisms for NSDI are suggested. The contributions of these mechanisms to the longitudinal ion momentum distributions are also analyzed. The present quantum mechanical QRS calculation verifies the validity of rescattering model for the NSDI processes at the most fundamental and detailed level.

I. INTRODUCTION

Nonsequential double ionization (NSDI) of atoms by linearly polarized laser pulses is one of the most interesting and challenging topics in strong-field physics. It represents a unique example where electron-electron interaction plays an essential role in the presence of a strong laser field. While the phenomena have been understood qualitatively based on the rescattering model [1,2], a full quantum mechanical theory for the complete quantitative description of the NSDI, even for a helium atom target, is still lacking. According to the rescattering model, an electron is first set free near the maximum of the oscillating electric field. Subsequently, it is driven back to the parent ion when the field changes direction, either to ionize or excite the second electron. If the second electron is excited, later it is easily released to the continuum when the laser's electric field increases again. Both processes result in the emission of two free electrons after the pulse is over. Since the 1990s, partial information on NSDI has been obtained experimentally from measuring the total yields, or the momentum distributions, of the resulting doubly charged ions [3–9]. Many such measurements have been reported for rare-gas atoms and for molecules using lasers of different intensities and different wavelengths. Since the 2000s, more complete measurements on the full momentum vectors of the two outgoing electrons have become available [10–17]. So far, such experiments have been reported only for 800-nm lasers, and often only the longitudinal momentum distributions (with respect to the laser's polarization axis) of the two electrons are presented. These latter data pose the ultimate challenge for our theoretical understanding of the NSDI processes.

Over the past two decades, there have been no shortage of theoretical efforts aiming at the NSDI processes. Since both the strong field of the laser as well as of the electron-electron interaction cannot be treated as perturbations, most of the theoretical efforts are based on some approximations. Using pure numerical approaches, they are either solved using a classical equation of motion [18] or using quantum mechanics with reduced dimensions [15,19–21]. Clearly, for pure numerical methods it is desirable to obtain an "exact" numerical solution of the time-dependent Schrödinger equation (TDSE) of the helium atom in the laser field. Unfortunately, such calculations have been reported so far for only helium atoms exposed to a 390-nm laser pulse [22]. For lasers of longer wavelengths, even the common 800-nm Ti:Sapphire laser, these calculations are still not possible with the present-day computers. For the full TDSE calculations, to obtain correlated electron-momentum distributions, one also has to project out the momentum wave function of the two continuum electrons, which by itself is not a trivial task.

The numerical methods discussed in the previous paragraph do not rely on the rescattering concept of NSDI outlined earlier. For theories that are based on such an idea, the so-called S-matrix theory was first employed [23–27]. This is a quantum perturbative expansion method starting with the "strong-field approximation." In this theory, the full electron-nucleus and electron-electron interactions are treated as the perturbation. Realistically, such theoretical calculations cannot be carried out beyond the second order. This means that all the electron-nucleus and electron-electron interactions have been included to first order only. Other approaches based on the rescattering model include treating tunneling ionization of the first electron quantum mechanically, but treating the propagation and the collision of the returning electron with the parent ion classically [28,29]. Such methods require additional modeling of the classical phase space of the second bound electron in the initial state and in the excited state after the excitation process.

In this paper, we present a full quantum theory of the NSDI processes based on the rescattering model. In the laser field,

an electron is first released by tunneling ionization from the atom. This electron may be driven back and accelerated by the electric field of the laser to revisit its parent ion as its phase changes subsequently. According to the rescattering model, these returning electrons can knock out or excite another electron to an excited state, analogous to the $(e, 2e)$ and electron-impact excitation processes, respectively. Since these processes occur in the laser field, each outgoing electron will acquire an additional momentum from the laser field. For the excited electron, it can be tunnel ionized by the laser field at a later time and emerges as a free electron as well. The additional momentum gained by each electron from the laser field is governed by the vector potential of the laser at the time when the electron is released. Using such a rescattering model, the momentum range of the two electrons and of the recoil ion can be understood based simply on the collision kinematics alone [11], that is, independent of the electron dynamics of the atom in the laser field. To go beyond this simple qualitative description, however, the theory has to be extended to the next level where quantitative calculations can be performed.

It is well recognized that NSDI is just one of the important rescattering phenomena when an atom is placed in a strong laser field. High-order harmonic generation (HHG) and high-energy above-threshold ionization (HATI) are also understood as resulting from the interaction of the returning electrons with the parent ion. In HHG, the returning electrons recombine with the target ion with the emission of high-energy photons. In HATI, the returning electrons are backscattered by the parent ion and emerge as high-energy photoelectrons, gaining additional momentum from the laser field after the scattering. In our recent works, we have shown that both HATI and HHG spectra can be accurately calculated using the so-called quantitative rescattering theory (QRS) [30–33]. Using QRS, HHG yields can be expressed as the product of a returning electron wave packet multiplied by the field-free photo-recombination cross sections [31,32]. Similarly, HATI spectra can be expressed as the product of a returning electron wave packet multiplied by field-free differential elastic scattering cross sections [30]. Both HHG and HATI processes can be viewed as one-electron phenomena in the interaction of the returning electron with the ion core. For NSDI, it involves electron-electron interaction, thus its theoretical treatment becomes more complicated. Similar to our earlier works on HATI and HHG spectra, in this paper our goal is to demonstrate how to apply the QRS model to NSDI processes. In an earlier work, the QRS model has been applied to evaluate the dependence of the total NSDI yields versus laser intensity for Ar [34]. In this paper, we generalize the theory to obtain the full electron-momentum distributions of the two outgoing electrons. Such calculations would allow us to compare with the most complete NSDI measurements, thus testing the rescattering model employed at the most fundamental level. The basic theoretical ingredients are presented in Sec. II. Since both $(e, 2e)$ and electron-impact excitation processes are involved in the final NSDI electron spectra, we first address the theories used for these collisions under the field-free conditions. We then discuss how these theories can be modified in the presence of the laser field. In Sec. III, we apply the QRS to study the correlated electron-momentum spectra of helium, employing laser parameters used in Staudte *et al.* [15], by analyzing the contributions

from the $(e, 2e)$ direct ionization processes, as well as from the indirect excitation-tunneling ionization processes. The results based on the QRS model are then compared to the correlated momentum spectra reported by Staudte *et al.* [15] using different models of the $(e, 2e)$ collisions. From the correlated electron-momentum spectra, we also obtain the longitudinal momentum spectra of the He^{2+} ions, which also can be compared to experimental measurements. Through such calculations we find that some features of the experimental correlated momentum spectra cannot be accounted for by either the $(e, 2e)$ or the excitation-tunneling mechanisms. We are thus drawn to suggest additional NSDI processes to interpret the remaining observed experimental features. The first is capture tunneling where the returning electron excites the core electron and itself is captured, thus forming doubly excited states. In the laser field, these two electrons are tunnel ionized subsequently before they have the chance to autoionize, thus contributing to double ionization signals. The other process is double ionization of the ground state by multiphoton process, or possibly single ionization followed by shakeoff. In both cases, rescattering is not involved. Such processes are characterized by low-energy electrons, as well as small recoil-ion momentum distributions. These mechanisms are discussed in Sec. III C. The ion-momentum spectra from the different NSDI processes are then addressed in Sec. III D. In Sec. IV, we provide a summary and discussion on what we consider the remaining issues of the present QRS theory for the NSDI processes.

II. THEORETICAL METHODS

A. Theoretical models for laser-free $(e, 2e)$ processes

Let $\mathbf{r}_1$ and $\mathbf{r}_2$ be the position vectors for the projectile and the bound-state electron, respectively, then the exact Hamiltonian for the whole system is

$$H = -\frac{1}{2}\nabla_1^2 - \frac{Z_N}{r_1} - \frac{1}{2}\nabla_2^2 - \frac{Z_N}{r_2} + \frac{1}{r_{12}}. \tag{1}$$

(Atomic units are used in this paper unless otherwise specified.) This Hamiltonian can be rewritten approximately as

$$H_i = -\frac{1}{2}\nabla_1^2 + U_i(r_1) - \frac{1}{2}\nabla_2^2 - \frac{Z_N}{r_2}, \tag{2}$$

where we assume that the He^+ ion initially is in the ground state and the charge of the nucleus is $Z_N = 2$. In this equation, $U_i(r_1)$ is the initial state distorting potential, which is used to calculate the initial state wave function for the projectile. Using the prior form, the direct transition amplitude for the $(e, 2e)$ collision process is expressed by

$$f_{e2e}(\mathbf{k}_1, \mathbf{k}_2) = \left\langle \Psi^-_{\mathbf{k}_1, \mathbf{k}_2} \middle| V_i \middle| \Psi_{\mathbf{k}_i} \right\rangle \tag{3}$$

where V_i is the perturbation interaction,

$$V_i = H - H_i = \frac{1}{r_{12}} - \frac{Z_N}{r_1} - U_i(r_1). \tag{4}$$

In Eq. (3), $\Psi^-_{\mathbf{k}_1, \mathbf{k}_2}$ is an exact solution of the three-body problem satisfying the incoming-wave boundary condition, that is,

$$(H - E_f)\Psi^-_{\mathbf{k}_1, \mathbf{k}_2}(\mathbf{r}_1, \mathbf{r}_2) = 0, \tag{5}$$

where $\mathbf{k}_1$ and $\mathbf{k}_2$ are the momenta of the two outgoing electrons detected in coincidence, and

$$E_f = \tfrac{1}{2}k_1^2 + \tfrac{1}{2}k_2^2. \tag{6}$$

Since the exact solution of Eq. (5) is not known analytically, various approximations will be used. First, we consider the theoretical model proposed by Brauner, Briggs, and Klar (BBK) [35], where the final continuum state is expressed as

$$\Psi_{\mathbf{k}_1,\mathbf{k}_2}^{-}(\mathbf{r}_1,\mathbf{r}_2) = (2\pi)^{-3} \exp(i\mathbf{k}_1 \cdot \mathbf{r}_1)\exp(i\mathbf{k}_2 \cdot \mathbf{r}_2) \\ \times C(\alpha_1,\mathbf{k}_1,\mathbf{r}_1)C(\alpha_1,\mathbf{k}_2,\mathbf{r}_2)C(\alpha_{12},\mathbf{k}_{12},\mathbf{r}_{12}), \tag{7}$$

where the Coulomb part of the wave function is defined as

$$C(\alpha,\mathbf{k},\mathbf{r}) = \exp(-\pi\alpha/2)\Gamma(1-i\alpha)\,_1F_1[i\alpha;1;-i(kr+\mathbf{k}\cdot\mathbf{r})] \tag{8}$$

and

$$\mathbf{k}_{12} = \tfrac{1}{2}(\mathbf{k}_1 - \mathbf{k}_2), \quad \mathbf{r}_{12} = \mathbf{r}_1 - \mathbf{r}_2, \\ \alpha_1 = -\frac{Z_N}{k_1}, \quad \alpha_2 = -\frac{Z_N}{k_2}, \quad \alpha_{12} = \frac{1}{2k_{12}}. \tag{9}$$

In Eq. (7), the Coulomb interaction between the two outgoing electrons has been taken into account. This interaction can be turned off by setting $\alpha_{12} = 0$. In Eq. (8), Γ is the gamma function and $_1F_1$ is the confluent hypergeometric function.

The initial state $\Psi_{\mathbf{k}_i}$ in Eq. (3) satisfies

$$(H_i - E_i)\Psi_{\mathbf{k}_i}(\mathbf{r}_1,\mathbf{r}_2) = 0, \tag{10}$$

where $\mathbf{k}_i$ is the incident momentum. The initial state wave function $\Psi_{\mathbf{k}_i}(\mathbf{r}_1,\mathbf{r}_2)$ in Eq. (10) can be written in the product form

$$\Psi_{\mathbf{k}_i}(\mathbf{r}_1,\mathbf{r}_2) = \varphi_{\mathbf{k}_i}(\mathbf{r}_1)\phi_{\mathrm{He}^+}(\mathbf{r}_2), \tag{11}$$

where $\varphi_{\mathbf{k}_i}(\mathbf{r}_1)$ describes the incident electron and satisfies

$$\left[-\tfrac{1}{2}\nabla_1^2 + U_i(r_1) - \tfrac{1}{2}k_i^2\right]\varphi_{\mathbf{k}_i}(\mathbf{r}_1) = 0, \tag{12}$$

and $\phi_{\mathrm{He}^+}(\mathbf{r}_2)$ is an eigenfunction of the equation

$$\left(-\frac{1}{2}\nabla_2^2 - \frac{Z_N}{r_2} - \epsilon_i\right)\phi_{\mathrm{He}^+}(\mathbf{r}_2) = 0. \tag{13}$$

The ground state wave function of He^+ is taken to be

$$\phi_{\mathrm{He}^+}(\mathbf{r}_2) = \left(\frac{Z_N^3}{\pi}\right)^{1/2}\exp(-Z_N r_2), \tag{14}$$

with the corresponding energy $\epsilon_i = -I_p$ where I_p is the ionization potential.

From Eqs. (10)–(13), we have

$$E_i = \epsilon_i + \tfrac{1}{2}k_i^2. \tag{15}$$

Due to energy conservation, $E_i = E_f$, we have

$$\tfrac{1}{2}k_i^2 = \tfrac{1}{2}k_1^2 + \tfrac{1}{2}k_2^2 + I_p. \tag{16}$$

The distorting potential $U_i(r_1)$ in Eq. (12) is not determined by the formalism. If we choose $U_i(r_1) = 0$, a plane wave is

obtained to describe the incident electron, that is,

$$\varphi_{\mathbf{k}_i}(\mathbf{r}_1) = \frac{1}{(2\pi)^{3/2}}\exp(i\mathbf{k}_i \cdot \mathbf{r}_1). \tag{17}$$

On the other hand, a Coulomb wave is an eigenfunction of Eq. (12) if one sets $U_i(r_1) = -(Z_N - 1)/r_1$, that is,

$$\varphi_{\mathbf{k}_i}(\mathbf{r}_1) = \frac{1}{(2\pi)^{3/2}}\exp(-\pi\alpha_i/2)\Gamma(1+i\alpha_i) \\ \exp(i\mathbf{k}_i \cdot \mathbf{r}_1)\,_1F_1[-i\alpha_i;1;i(k_i r_1 - \mathbf{k}_i \cdot \mathbf{r}_1)], \tag{18}$$

where $\alpha_i = -(Z_N - 1)/k_i$.

Finally, the triple differential cross section (TDCS) for electron-impact ionization process is given by [36]

$$\frac{d^3\sigma_{e2e}}{d\Omega_1 d\Omega_2 dE} = (2\pi)^4\frac{k_1 k_2}{k_i}\left[\frac{3}{4}|f_{e2e}(\mathbf{k}_1,\mathbf{k}_2) - g_{e2e}(\mathbf{k}_1,\mathbf{k}_2)|^2 \\ + \frac{1}{4}|f_{e2e}(\mathbf{k}_1,\mathbf{k}_2) + g_{e2e}(\mathbf{k}_1,\mathbf{k}_2)|^2\right], \tag{19}$$

where $\Omega_1(\theta_1,\phi_1)$ and $\Omega_2(\theta_2,\phi_2)$ are the solid angles of detection of the two electrons leaving the collision with momenta $\mathbf{k}_1$ and $\mathbf{k}_2$, and $g_{e2e}(\mathbf{k}_1,\mathbf{k}_2)$ is the exchange amplitude with $g_{e2e}(\mathbf{k}_1,\mathbf{k}_2) = f_{e2e}(\mathbf{k}_2,\mathbf{k}_1)$.

Based on the general expression Eq. (19), we can now consider a few approximations that are often used in the field-free $(e,2e)$ collisions. These are as follows: (i) The P-CC model, in which the incident electron is represented by a plane wave and the two continuum electrons in the final state are represented by the product of two Coulomb functions. The latter is obtained from Eq. (7) by setting $\alpha_{12} = 0$. (ii) The P-CCC model, in which the incident electron is approximated by a plane wave but the final two-electron continuum wave function is the product of three Coulomb functions, as in the BBK model [35], that is, Eq. (7). Clearly, for an electron colliding with a He^+ ion, the electron experiences a Coulomb potential asymptotically; thus, a Coulomb wave, Eq. (18), would be more appropriate. Thus one can carry out C-CC or C-CCC approximations. In the BBK model, the interaction between each pair of charges is not screened by the presence of the third charge. This deficiency was first corrected by Berakdar and Briggs [37], by introducing effective Sommerfeld parameters for the case in which the two outgoing electrons have equal energies. The model was later generalized by Chen *et al.* [38] for any geometry and energy sharing. Such a modification represents a dynamic screening (DS) of the three-body Coulomb interactions, and hence the improved BBK model is called DS3C. The details of the DS3C and its improvement over the BBK model when compared to the experimental TDCS for electron-impact ionization of atomic hydrogen can be found in Chen *et al.* [38]. In this paper, we consider the P-CC, P-CCC, and P-DS3C models only. Calculations based on C-CCC and C-DS3C are much more complicated and are not investigated in this work.

The TDCS in Eq. (19) is spin averaged for the usual $(e,2e)$ collisions. We have used Eq. (19) in our previous TDCS calculations for the NSDI of helium [39]. However, the returning electron initially is in the helium atom, and the two electrons are in the singlet spin state. Since the total

spin is preserved during ionization [40], the TDCS should be given by

$$\frac{d^3\sigma_{e2e}^{\text{Singlet}}}{d\Omega_1 d\Omega_2 dE} = (2\pi)^4 \frac{k_1 k_2}{k_i} |f_{e2e}(\mathbf{k}_1,\mathbf{k}_2) + g_{e2e}(\mathbf{k}_1,\mathbf{k}_2)|^2. \tag{20}$$

B. Theoretical models for laser-free electron-impact excitation processes

Different from the $(e,2e)$ process, the final unperturbed state of the total system for electron-impact excitation of He$^+$ is given by

$$\Phi_{\mathbf{k_f}}^-(\mathbf{r}_1,\mathbf{r}_2) = \varphi_{\mathbf{k_f}}^-(\mathbf{r}_1)\phi_f(\mathbf{r}_2), \tag{21}$$

where $\varphi_{\mathbf{k_f}}$ is the wave function used to describe the outgoing electron, which satisfies the differential equation

$$\left(-\tfrac{1}{2}\nabla_1^2 + U_f(r_1)\right)\varphi_{\mathbf{k_f}}(\mathbf{r}_1) = \tfrac{1}{2}k_f^2 \varphi_{\mathbf{k_f}}(\mathbf{r}_1). \tag{22}$$

For the present purpose, we set the distorting potential $U_f(r_1) = -(Z_N - 1)/r_1$ such that the scattered outgoing electron is described by a Coulomb wave.

The final excited state $\phi_f(\mathbf{r}_2)$ satisfies

$$\left(-\frac{1}{2}\nabla_2^2 - \frac{Z_N}{r_2} - \epsilon_n\right)\phi_f(\mathbf{r}_2) = 0, \tag{23}$$

where $\epsilon_n = -0.5Z_N^2/n^2$ is the energy of the excited state.

The T-matrix element for a transition from an initial state to a final state is then given by

$$f_{\text{exci}} = \langle \varphi_{\mathbf{k_f}}^-(\mathbf{r}_1)\phi_f(\mathbf{r}_2)|V_i|\varphi_{\mathbf{k_i}}(\mathbf{r}_1)\phi_i(\mathbf{r}_2)\rangle, \tag{24}$$

where V_i is given by Eq. (4). The differential cross section (DCS) for this transition is given by

$$\frac{d\sigma_{\text{exci}}}{d\Omega} = (2\pi)^4 \frac{k_f}{k_i}\left(\frac{3}{4}|f_{\text{exci}} - g_{\text{exci}}|^2 + \frac{1}{4}|f_{\text{exci}} + g_{\text{exci}}|^2\right), \tag{25}$$

where the exchange amplitude g_{exci} is calculated from

$$g_{\text{exci}} = \langle \varphi_{\mathbf{k_f}}^-(\mathbf{r}_2)\phi_f(\mathbf{r}_1)|V_i|\varphi_{\mathbf{k_i}}(\mathbf{r}_1)\phi_i(\mathbf{r}_2)\rangle. \tag{26}$$

In our actual calculations, a Coulomb wave is also used to describe the incident electron; that is, $\varphi_{\mathbf{k_i}}(\mathbf{r}_1)$ in Eqs. (24) and (26) is expressed by Eq. (18).

Due to the same spin-conservation reason stated in the previous section, the DCS for electron-impact excitation of He$^+$ in the laser field should be expressed as

$$\frac{d\sigma_{\text{exci}}^{\text{Singlet}}}{d\Omega} = (2\pi)^4 \frac{k_f}{k_i}|f_{\text{exci}} + g_{\text{exci}}|^2. \tag{27}$$

C. Quantitative rescattering theory for laser-induced $(e,2e)$ processes

According to the QRS model [30], for laser-induced single ionization at single peak intensity I, the momentum distribution $D(I,p,\theta)$ for high-energy photoelectron with momentum p at an outgoing angle θ with respect to the

polarization, which is taken to be the $+z$ axis, can be expressed as

$$D(I,p,\theta) = W(I,k_r)\sigma(k_r,\theta_r). \tag{28}$$

Here $\sigma(k_r,\theta_r)$ is the elastic differential cross sections between free electrons, with momentum k_r, with the target ion, and θ_r is the scattering angle with respect to the direction of the returning electrons along the laser polarization axis. In Eq. (28), $W(I,k_r)$ is called the returning wave packet, which can be interpreted as the momentum distribution of the returning electron beam.

The photoelectron momentum $\mathbf{p}$ and the momentum $\mathbf{k}_r$ of the electron after scattering with the parent ion are related by

$$\mathbf{p} = \mathbf{k}_r - \mathbf{A}_r, \tag{29}$$

where $\mathbf{A}_r$ is the vector potential at the time when electrons return to the origin. In addition, based on the classical simulation [30], the QRS relates

$$k_r = 1.26|A_r|. \tag{30}$$

The projections of the photoelectron momentum in the parallel and perpendicular directions are

$$p^{||} = p\cos\theta = -A_r - k_r\cos\theta_r = -A_r + k_r^{||}, \\ p^{\perp} = p\sin\theta = k_r\sin\theta_r = k_r^{\perp}. \tag{31}$$

To study the laser-induced $(e,2e)$ process, we recognize that the recollision electron, which is first tunnel ionized in the laser pulse and then driven back to collide again with the parent ion, is actually the incident electron with momentum $\mathbf{k}_i$. Thus

$$k_i = k_r. \tag{32}$$

In the correlated two-electron momentum spectra induced in a strong laser field, experimentalists reported only the momentum components of the two electrons along the laser polarization axis. Thus we integrate the TDCS, for laser-free $(e,2e)$ process at a given incident energy $E_i = k_i^2/2$, over ϕ_2 and E_2

$$Y_{E_i}^{e,2e}(k_1^{||},k_2^{||}) = \frac{4\pi}{k_1 k_2}\int_0^{E_{\max}} dE_2 \int_0^\pi d\phi_2 \frac{d^3\sigma_{e2e}^{\text{Singlet}}}{d\Omega_1 d\Omega_2 dE_2}\Big|_{\phi_1=0}, \tag{33}$$

where $E_{\max} = E_i - I_p$. In Eq. (33), we set $\phi_1 = 0$ due to the cylindrical symmetry. In the actual calculations, the integration over ϕ_2 is performed only from 0 to π since the TDCS is symmetric about the plane containing $\mathbf{k}_1$ and $\mathbf{k}_i$.

To obtain the correlated two-electron momentum spectra at an incident energy of E_i for NSDI in a strong field, the only thing we need to do is to shift the momentum by using the relation in (29), that is,

$$D_{E_i}^{e,2e}(p_1^{||},p_2^{||}) = Y_{E_i}^{e,2e}(k_1^{||},k_2^{||}). \tag{34}$$

Similar to (28), the final distribution can be evaluated by

$$D_{e,2e}(p_1^{||},p_2^{||}) = \int_{I_p}^\infty dE_i \, D_{E_i}^{e,2e}(p_1^{||},p_2^{||})\bar{W}(E_i), \tag{35}$$

where $\bar{W}(E_i)$ is the volume-integrated wave packet [30], that is, the wave packet integrated over the volume distribution of the laser pulse at peak intensity I_0,

$$\bar{W}(E_i) = \rho \int_0^{I_0} W(I,E_i)\left(\frac{\partial V}{\partial I}\right)dI, \tag{36}$$

where $W(I,E_i)$ is the wave packet of the returning electron with energy $E_i = k_r^2/2$ in the laser field at single peak intensity of I, $(\partial V/\partial I)dI$ represents the volume of an isointensity shell between I and $I + dI$ defined in [41] for a Lorentzian (propagation direction) and a Gaussian (transverse direction) beam profile, and ρ is the density of atoms in the chamber. The temporal profiles of the laser pulses used in the simulation are discussed later. We also comment that in our calculation, the depletion effect is always included in the calculation of the wave packet.

D. Quantitative rescattering theory for laser-induced excitation-tunneling processes

Similar to the laser-free $(e,2e)$ process, to compare with the measured correlated momentum spectra along the polarization direction, one needs to project the differential cross section for electron-impact ionization onto the polarization direction and integrate over perpendicular components. Since the differential cross section is symmetric about the incident direction, for a given incident energy, this integral can be simply performed as

$$Y_{E_i}^{\text{exci}}(k_f^{||}) = \frac{2\pi}{k_f}\frac{d\sigma_{\text{exci}}^{\text{Singlet}}}{d\Omega}. \quad (37)$$

According to the QRS model, the laser-free momentum spectra should be shifted by $-A_r$, which is the vector potential at the moment when the recollisional electron returns to the parent ion. Without loss of generality, one may assign 1 to the projectile in the final state. Consequently, the momentum spectra for electron-impact excitation at a fixed incident energy in a strong laser field is given by

$$D_{E_i}^{\text{exci}}(p_1^{||}) = Y_{E_i}^{\text{exci}}(k_f^{||}). \quad (38)$$

As mentioned earlier, since an excited electron is readily ionized in the strong laser field, the rate of ionization of the excited electron has to be considered. We evaluate the ionization rate by static-tunneling ionization theory, which is also the basis of the Ammosov-Delone-Krainov (ADK) theory [42]. Since excitation takes place at the time when the electric field is near zero, this is the moment from which tunneling ionization begins. Therefore, at time t, the tunneling ionization rate for an excited electron in the laser pulse with a single peak intensity I is given by

$$Y_{E_i}^{\text{adk}}(I,t) = w\left[|F(t)|\right]e^{-\int_{t_r}^{t} w[|F(t)|]dt}. \quad (39)$$

We use a linearly polarized laser pulse such that the electric field in Eq. (39) is taken as

$$\mathbf{F}(t) = F_0 a(t)\cos(\omega t + \phi)\hat{z}, \quad (40)$$

where ω is the frequency of the carrier wave and ϕ is the carrier envelope phase with the envelope function $a(t)$ chosen to be

$$a(t) = \cos^2\left(\frac{\pi t}{\tau}\right) \quad (41)$$

for the time interval $(-\tau/2, \tau/2)$ and zero elsewhere.

The modified ADK rate $w[|F(t)|]$ in Eq. (39) is given by [43]

$$w[|F(t)|] = \beta\frac{C_l^2}{2^{|m|}|m|!}\frac{(2l+1)(l+|m|)!}{2(l-|m|)!}\frac{1}{\kappa^{2Z_c/\kappa-1}} \\ \times \left(\frac{2\kappa^3}{|F(t)|}\right)^{2Z_c/\kappa-|m|-1}e^{-2\kappa^3/3|F(t)|}, \quad (42)$$

where β is a correction factor introduced empirically by Tong and Lin [43],

$$\beta = e^{-\mu(Z_c^2/I_p)(|F(t)|/\kappa^3)}, \quad (43)$$

with $\kappa = \sqrt{2I_p}$, and Z_c is the charge of the residual ion. In Eq. (42), l and m are the usual angular momentum quantum numbers of the valence electron of the atom, and C_l measures the amplitude of the electron wave function in the tunneling region, which can be determined by the asymptotic behavior of the wave function of the electron in the bound state from which it is ionized [44]. The parameter μ in Eq. (43) is set to be $6 < \mu < 12$ for the cases considered here. In Eq. (39), t_r is chosen to be the time when $A_r \equiv A(t_r) = k_r/1.26$. From Eq. (39), we mention that the depletion of the excited state has been explicitly considered.

The momentum spectra of the excited electron after tunneling ionization at the end of the laser pulse is obtained by shifting the initial momentum by the drift momentum, which is the vector potential at the time it is ionized. Since the initial velocity of the tunneling electron can be neglected, one obtains the momentum spectra for electron 2 as

$$D_{E_i}^{\text{adk}}(I,p_2^{||}) \equiv D_{E_i}^{\text{adk}}[I,-A(t)] = Y_{E_i}^{\text{adk}}(I,t). \quad (44)$$

Note that this equation relates the momentum of electron 2 to the time when it is ionized. The momentum distributions in $p_2^{||}$ reflects the time dependence of tunnel ionization.

By taking into account the focal volume effect, the correlated momentum spectra for a fixed energy is then given by

$$D_{E_i}^{\text{exci-tun}}(p_1^{||},p_2^{||}) = D_{E_i}^{\text{exci}}(p_1^{||})D_{E_i}^{\text{adk}}(I_0,p_2^{||}) \quad (45)$$

with

$$D_{E_i}^{\text{adk}}(I_0,p_2^{||}) = \rho\int_0^{I_0} W(I,E_i)D_{E_i}^{\text{adk}}(I,p_2^{||})\left(\frac{\partial V}{\partial I}\right)dI. \quad (46)$$

The final distribution can be obtained by

$$D_{\text{exci-tun}}(p_1^{||},p_2^{||}) = \int_{I_{\text{exci}}}^{\infty} dE_i D_{E_i}^{\text{exci-tun}}(p_1^{||},p_2^{||}), \quad (47)$$

where I_{exci} is the excitation energy.

E. Kinematical analysis of the correlated electron-momentum spectra

First we consider the kinematics of the field-free $(e,2e)$ process. In Fig. 1, the $(e,2e)$ kinematics in the coplanar geometry is illustrated. In the laser field, the recollision electron can be driven back in two directions along the polarization axis. When the electron tunnels out after the peak of the electric field when $E(t) > 0$, it will be driven back along $+\hat{z}$. This process is shown in Figs. 1(a) and 1(b). The projectile electron is mostly scattered into the forward direction. For binary collisions, according to momentum conservation, $k_2^{\perp} = -k_1^{\perp}$ and the two
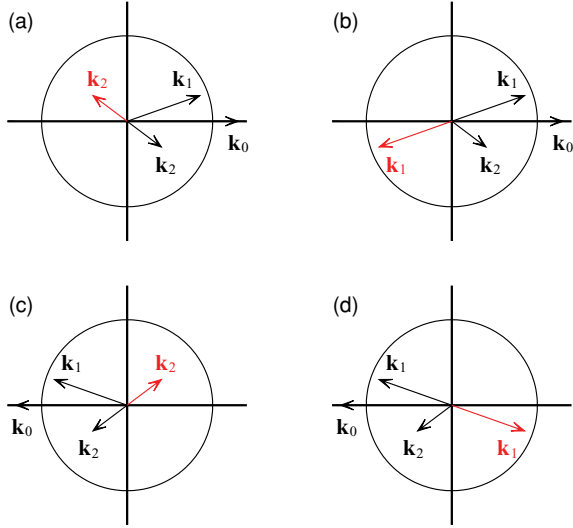
FIG. 1. (Color online) Geometry of electron-momentum vectors in laser-free $(e,2e)$ process. The circles indicate the maximum momentum.
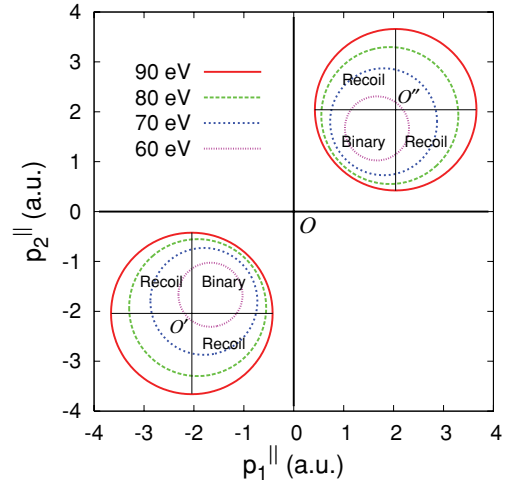

FIG. 2. (Color online) Kinematically allowed region of the photoelectron momentum components parallel to the laser polarization axis of the two outgoing electrons in the recollisional $(e,2e)$ process of He$^+$ at incident energies of 60, 70, 80, and 90 eV, respectively.

electrons lie in the momentum regime of $(k_1^{||} > 0, k_2^{||} > 0)$. On the other hand, recoil collisions do take place if the bound electron is not ejected directly but is backscattered by the nucleus sequentially before it is ejected. This corresponds to the momentum regime of $(k_1^{||} > 0, k_2^{||} < 0)$, as illustrated in Fig. 1(a). Since the two outgoing electrons are indistinguishable, the two electrons can be interchanged. Figure 1(b) illustrates the same collision except that electron 2 with momentum $\mathbf{k}_2$ is regarded as the projectile while electron 1 with momentum $\mathbf{k}_1$ is the ejected one. In this case, the recoil collision regime is bound by $(k_1^{||} < 0, k_2^{||} > 0)$.

For a long pulse, the probability that the electron is ionized during $E(t) < 0$ is the same as that when $E(t) > 0$. In the case when the electron is born when $E(t) < 0$, the recollision electron comes back along $-\hat{z}$, as illustrated in Figs. 1(c) and 1(d). Consequently, the momentum regime of $(k_1^{||} < 0, k_2^{||} < 0)$ corresponds to the binary collision while the recoil collision has two possible regimes of $(k_1^{||} < 0, k_2^{||} > 0)$ and $(k_1^{||} > 0, k_2^{||} < 0)$.

For the $(e,2e)$ process occurring in the laser field, the parallel momentum of each electron is shifted by $-A_r$ as the electron exits the laser field. Here A_r is the vector potential at the time of the $(e,2e)$ collision. Figure 2 displays the kinematically allowed region of the momentum components of the photoelectrons parallel to the laser polarization for the two outgoing electrons due to the recollisional $(e,2e)$ process. According to Eq. (29), the center of the correlated momentum spectra is located in the third quadrant if the recollision electron returns to the parent ion along $+\hat{z}$. They correspond to the $(e,2e)$ collision geometry shown in Figs. 1(a) and 1(b). Similarly, the center of the momentum spectra for the collision geometry shown in Figs. 1(c) and 1(d) is located in the first quadrant. Using Eqs. (30) and (32), the center of the drift momentum is related to the incident energy (i.e., the returning electron energy) by

$$|A_r| = \sqrt{2E_i}/1.26, \qquad (48)$$

and the allowed region of the correlated momentum spectra is restricted to a circle whose radius is determined by

$$r = \sqrt{2(E_i - I_p)} = \sqrt{(1.26 A_r)^2 - 2I_p}. \qquad (49)$$

In Fig. 2, O' and O'' indicate the momentum centers for an incident energy of 90 eV of recollision electron along $+\hat{z}$ and $-\hat{z}$, respectively. With respect to each center, the binary collisions occupy one quadrant, while the recoil collisions occupy two quadrants. The remaining quadrant is not allowed based on the $(e,2e)$ rescattering kinematics. In Fig. 2, we also show that the allowed $(e,2e)$ region shrinks as the returning electron energy is decreased.

We next consider the strong-field excitation-tunneling ionization process. For the laser-free electron-impact excitation process, at fixed incident energy E_i, the range of the parallel momentum of the scattered electron is $(-k_f^{\max}, k_f^{\max})$, where $k_f^{\max} = \sqrt{2(E_i - I_{\text{exci}})}$. While the excitation process takes place in the laser field, the projectile will exit the laser field with its parallel momentum restricted by $-k_f^{\max} - A_r \leqslant p_1^{||} \leqslant k_f^{\max} - A_r$. For the excited electron that is tunnel ionized, its parallel momentum is restricted by the drift momentum, that is, $(-|A_r| \leqslant p_2^{||} \leqslant |A_r|)$, since the electron tunnels out with zero initial velocity. Here, the maximum momentum occurs when the excited electron is tunnel ionized immediately after impact excitation. These conditions lead to the correlated parallel momentum spectra in the first and fourth quadrants for the case in which the recolliding electron returns to the origin along the $-\hat{z}$ direction, as illustrated by black rectangular areas in Fig. 3, for incident energies of 90 and 60 eV, respectively. On the other hand, if the returning electron is driven back along the $+\hat{z}$ direction, the correlated parallel momentum spectra will be located in the second and third quadrants as shown in Fig. 3. Furthermore, since the two outgoing electrons are indistinguishable, the correlated spectra should be symmetric with respect to both diagonals $p_1^{||} = \pm p_2^{||}$. Therefore, the other
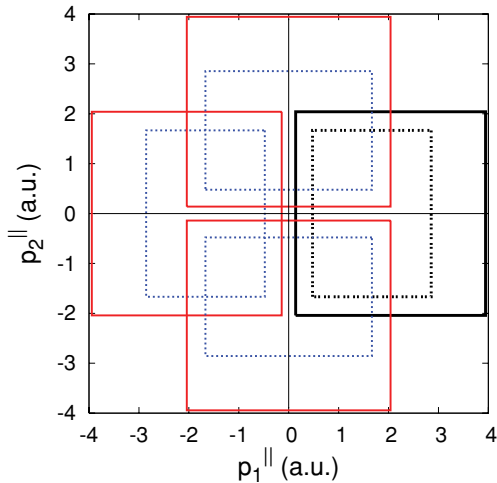
FIG. 3. (Color online) Kinematically allowed region of the photoelectron momentum components parallel to the laser polarization axis for the two outgoing electrons in the excitation-tunneling process. The rectangles in solid (dotted) lines are for electron excitation from the ground state of He^+ to the $n = 2$ state at incident energies of 90 eV (60 eV).

two areas for $p_2^{\parallel} > 0$ (in the first and second quadrants) and $p_2^{\parallel} < 0$ (in the third and fourth quadrants) are also allowed for the excitation-tunneling processes. Based on this kinematic analysis, it is clear from Figs. 2 and 3 that the correlated electron spectra in the second and forth quadrants are to be attributed to the excitation-tunneling ionization processes only.

It should be noted that a similar kinematic analysis of the constraints of correlation electron momentum spectra for the $(e,2e)$ and the excitation-tunneling ionization processes has been reported previously by Feuerstein *et al.* [11].

Recently, Staudte *et al.* [15] reported a kinematically complete experiment on NSDI of He by an 800-nm, 4.5×10^{14} W/cm^2 laser pulse. For the laser pulse used in the experiment, the ponderomotive energy $U_p = 27$ eV, and the

maximum energy that the returning electron accumulates in the laser field is $E_i^{\max} = 3.17U_p = 85.6$ eV. The measured correlated momentum spectra from Staudte *et al.* are shown in Fig. 4(a). Based on this analysis, the $(e,2e)$ events are located in the first and third quadrants only, while the excitation-tunneling events are distributed symmetrically in all four quadrants. Following Feuerstein *et al.* [11], by subtracting the corresponding number of excitation-tunneling events from the measured number of all events in the first and third quadrants, we obtain the correlated momentum distribution for the "pure" $(e,2e)$ process, which is displayed in Fig. 4(b). It should be noted that the original experiment spectra include contamination from the H_2^+ background as indicted by the lines in Fig. 4(a). This background should be removed to ensure that the spectra in the second and fourth quadrants are from the excitation-tunneling process only. The excitation-tunneling spectra are shown in Fig. 4(c).

F. Returning electron wave packets

The kinematic analysis restricts the range of momentum space allowed by the $(e,2e)$ and the excitation-tunneling ionization processes. To obtain the actual correlation momentum spectra, the $(e,2e)$ and excitation-tunneling ionization cross sections have to be weighted by the returning electron-momentum distributions generated by the laser pulse. Experimentally, a focused laser pulse does not have a uniform peak intensity. Rather the peak intensity is distributed within the focal volume. In order to compare with experiments, we need to take into account the volume effect. Within the QRS, this is routinely carried out. In fact, a returning wave packet including the volume effect is easily calculated; see Chen *et al.* [30]. In Fig. 5, the volume-integrated wave packets [30] are plotted for 800-nm pulses at peak intensities of 4.0, 4.5, and 5.0×10^{14} W/cm^2. It can be seen from Fig. 5 that the wave packets at different peak intensities have similar shape and they decrease as the momentum (energy) of the returning electron increases.
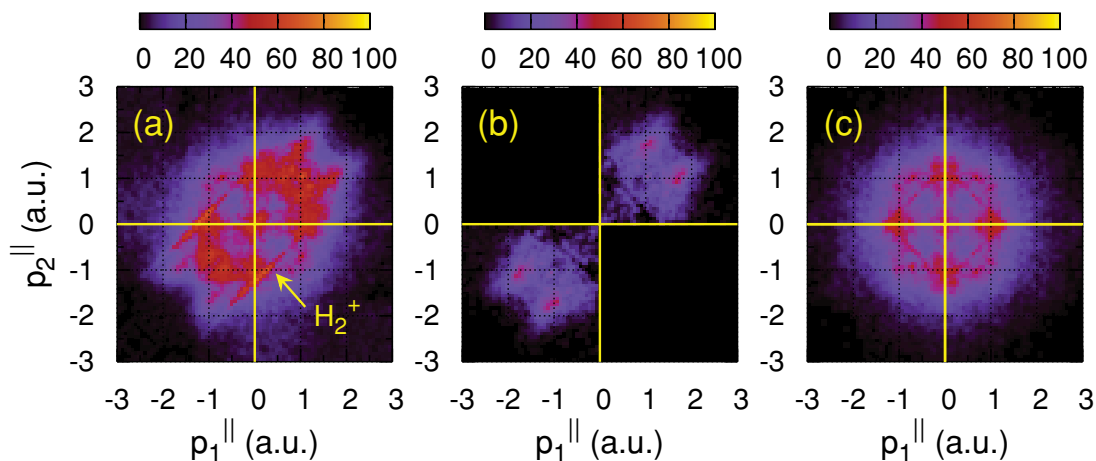

FIG. 4. (Color online) (a) Experimental correlated electron momentum spectra along the polarization direction for double ionization of helium by a laser with wavelength of 800 nm at an intensity of 4.5×10^{14} W/cm^2. The indicated lines are H_2^+ background from cold H_2 in the gas jet. (b) Same as (a), but only the $(e,2e)$ portion is retained. (c) Same as (a), only the excitation-tunneling portion [or more precisely, the non-$(e,2e)$ portion] is retained. The original data are from Staudte *et al.* [15].
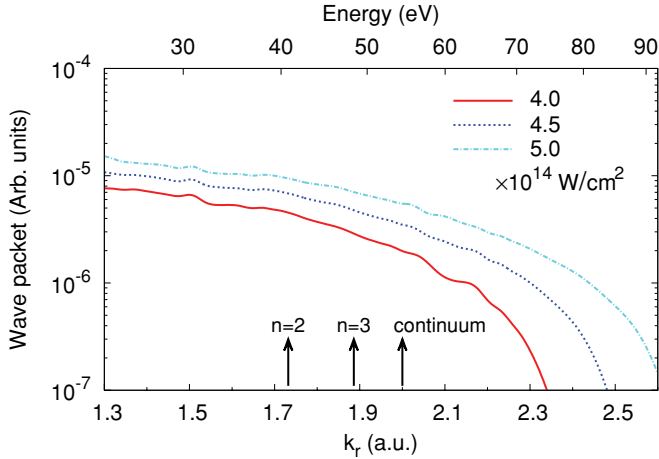
FIG. 5. (Color online) Wave packets (integrated over laser focus volume) against the momentum of the recollision electron (the bottom horizontal axis) for 45 fs full-width at half-maximum (FWHM) laser pulses at peak intensities of 4.0, 4.5, and 5.0×10^{14} W/cm², with a wavelength of 800 nm. The arrows indicate the minimum momentum for the recollision electron to excite the electron in the parent ion He$^+$ from $n = 1$ to $n = 2$ and $n = 3$ states, or to ionize the parent ion, respectively. The corresponding energy of the returning electron is also indicated on the top horizontal axis.

III. RESULTS AND DISCUSSION

A. Correlated electron spectra due to the $(e,2e)$ processes in strong laser fields

Based on the QRS model, we obtain the correlated two-electron momentum spectra using different field-free $(e,2e)$ collision theories introduced in Sec. II A. The results are to be compared to the data of Staudte *et al.*, in particular, the part that was attributed to the $(e,2e)$ collisions; see Fig. 4(b). First, we consider the case when the returning electron has a fixed energy of 85 eV, or $k_r = 2.5$. The correlated electron spectra obtained using the P-CC model and the P-CCC model are displayed in Figs. 6(a) and 6(b), respectively. The momentum spectra of the P-CC model appear like two half moons, with no clear minimum along the diagonal line connecting the first and third quadrants. From the analysis in Sec. II E, the main contribution to the correlated spectra in the P-CC model is due to binary collisions. On the other hand, the prediction based on the P-CCC model shows that recoil collisions dominate. The P-CCC model predicts little signals along the diagonal line in the first and third quadrants and shows fingerlike features that are much closer to the experimental data shown in Fig. 4(b). Such analysis clearly indicates that Coulomb repulsion between the two outgoing electrons is crucial in $(e,2e)$ collisions at the energy of 85 eV. Since the ionization energy of He$^+$ is 54.4 eV, after impact ionization, the two electrons have only about 30 eV to share between them. For such low-energy collisions, electron-electron interaction is expected to play an important role, as reflected by the large difference in the correlated electron spectra between the P-CC and P-CCC models.

To obtain correlated electron-momentum spectra that can be compared to the experimental data, the theoretical calculations should be integrated over the momentum distributions of the
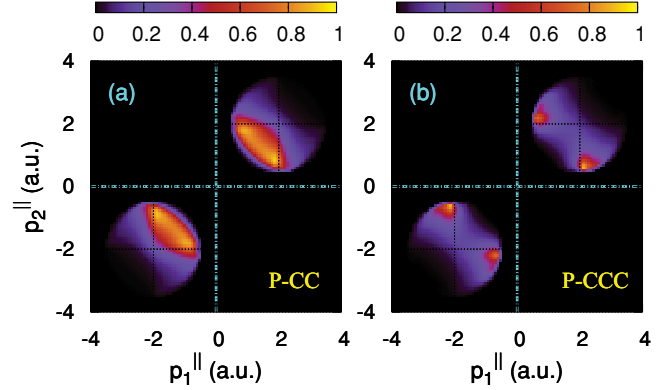
returning wave packet. For the 800-nm laser at peak intensity of 4.5×10^{14} W/cm² used by Staudte *et al.*, the returning electron wave packet is shown in Fig. 5, along with two other nearby intensities. In Fig. 7, we compare the volume-integrated momentum spectra of the theoretical simulations with experimental measurements taken from Fig. 4(b). Only spectra in the first quadrant are shown since the spectra in the third quadrant are symmetric with respect to the first quadrant.

The volume-integrated spectra of P-CC and P-CCC shown in Fig. 7 are slightly different from the results at the fixed incident returning energy shown in Fig. 6 while the main features remain the same. Again, different from the P-CC, the P-CCC predicts a fingerlike structure which is in better agreement with the experimental measurement. A comparison of P-DS3C versus P-CCC shows that the two separated peaks in the spectra of P-CCC are connected by a bridge
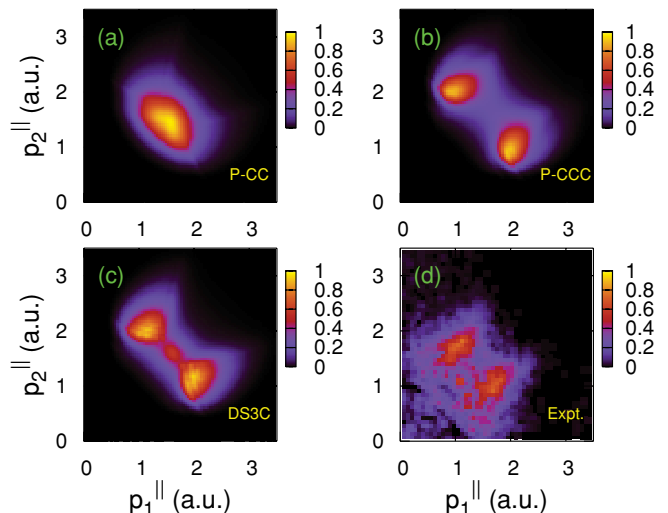

FIG. 6. (Color online) Theoretical normalized correlated momentum spectra for two outgoing electrons in the recollisional $(e,2e)$ process on He$^+$ at an incident electron energy of 85 eV. Shown are the momentum components along the polarization direction. The theoretical models used in the simulation are (a) P-CC and (b) P-CCC. See the text for details.

FIG. 7. (Color online) Momentum spectra for two outgoing electrons in the recollisional $(e,2e)$ process on He$^+$. Lasers are at 800 nm with intensity of 4.5×10^{14} W/cm². Shown are the momentum components along the polarization direction. The theoretical models used are (a) P-CC, (b) P-CCC, and (c) P-DS3C. (d) Experiment.
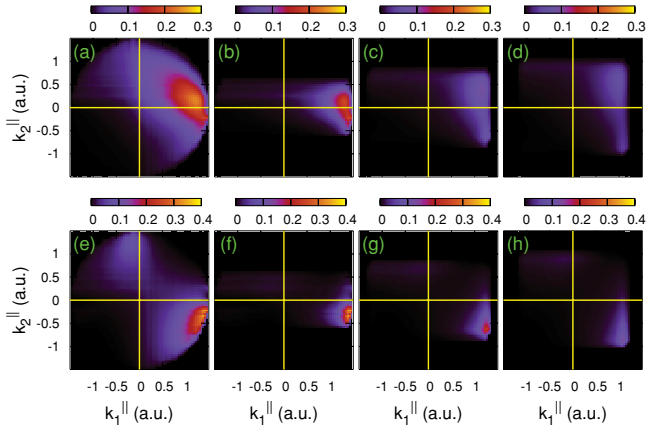
FIG. 8. (Color online) Momentum spectra from direct ionization amplitudes only for the two outgoing electrons in laser-free $(e,2e)$ process on He$^+$ at incident electron energy of 85 eV. Shown are the momentum components along the incident direction, which is taken to be $+\hat{z}$. The P-CC model is used for (a)–(d), and P-CCC is used for for (e)–(h). (a), (e) Final integrated spectra; Intermediate integrated spectra for (b), (f) $E_2 = (0-5)$ eV; (c), (g) $E_2 = (5-10)$ eV; and (d), (h) $E_2 = (10-15)$ eV.

in P-DS3C. This illustrates the effect of screening included in the P-DS3C model, which suppresses somewhat the strong electron-electron Coulomb repulsion.

To understand how the two electrons share the total available kinetic energy after the $(e,2e)$ process, we consider the situation where the incident electron comes along the $+\hat{z}$ direction, corresponding to laser-induced correlated momentum spectra in the third quadrant in Fig. 6. Since the final integrated ionization yields $Y_{E_i}^{e,2e}(k_1^{||},k_2^{||})$ in Eq. (33) from the direct amplitude $f(\mathbf{k}_1,\mathbf{k}_2)$ and the exchange amplitude $g(\mathbf{k}_1,\mathbf{k}_2)$ are identical, provided that the two electron indices are exchanged, we show only how the direct ionization yields depend on the energy of the ejected electron (electron 2), for the P-CC and P-CCC models, respectively. The total direct ionization yields in the two-electron momentum space for the two models are shown in Figs. 8(a) and 8(e), respectively. For the P-CC model, the distributions are mostly in the binary collision region (see the illustration in the third quadrant of Fig. 2), with minor components in the recoil collision region. In contrast, for the P-CCC model, the main distributions are in the recoil collision region. In Figs. 8(b)–8(d), the intermediate distributions integrated over different ejected electron energy ranges of 0–5, 5–10, and 10–15 eV are shown for the P-CC model, and in Figs. 8(f)–8(h), they are shown for the P-CCC model. In this example, the two electrons share a total energy of 30 eV. The intermediate results shown in Figs. 8(b)–8(d) and 8(f)–8(h) correspond to the asymmetric geometry in which one electron has higher energy than the other. It clearly shows that total momentum distributions are mainly coming from the low-energy part. This implies that highly asymmetric $(e,2e)$ processes make bigger contributions.

The TDCS provides the most detailed information about the $(e,2e)$ processes. To see the mechanism in a more direct way, we next focus on the TDCS for fixed $k_1^{||}$, corresponding to the traditional asymmetric geometry in which the energy and the scattering angle of the projectile in the final state are fixed while
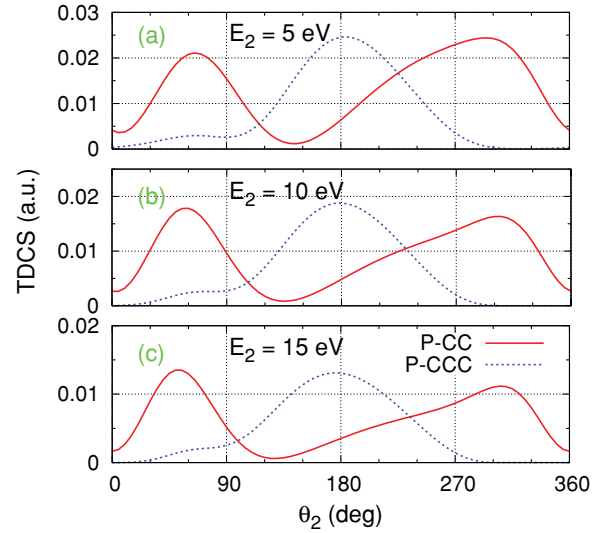

FIG. 9. (Color online) Triple differential cross sections from direct amplitude only for laser-free $(e,2e)$ process on He$^+$ at incident energy of 85 eV in the coplanar geometry for fixed $\theta_1 = 30°$ and ejected electron energies of (a) 5 eV, (b) 10 eV, and (c) 15 eV, respectively.

the scattering angle of the ejected electron varies from $0°$ to $360°$. Again, for $E_i = 85$ eV, we choose $k_1^{||} = 1.21$, 1.07, and 0.96 for $E_2 = 5$, 10, and 15 eV, respectively, corresponding to $\phi_1 = 0°$ and $\theta_1 = 30°$. The TDCS as function of θ_2 are shown in Fig. 9. Here we set $\phi_2 = 180°$. The corresponding coplanar $(e,2e)$ geometry is illustrated in Fig. 10.

In Fig. 9, the TDCS for $\theta_2 < 90°$ and $\theta_2 > 270°$ corresponds to the spectra for $k_2^{||} > 0$ in the first quadrant, while that for $90° < \theta_2 < 270°$ corresponds to the spectra for $k_2^{||} < 0$ in the forth quadrant in Fig. 8. It can be seen in Fig. 9 that a strong binary peak is reproduced in the P-CC calculations when $\theta_2 < 90°$, corresponding to the geometry displayed in Fig. 10(a). The binary peak shifts to a smaller angle when the

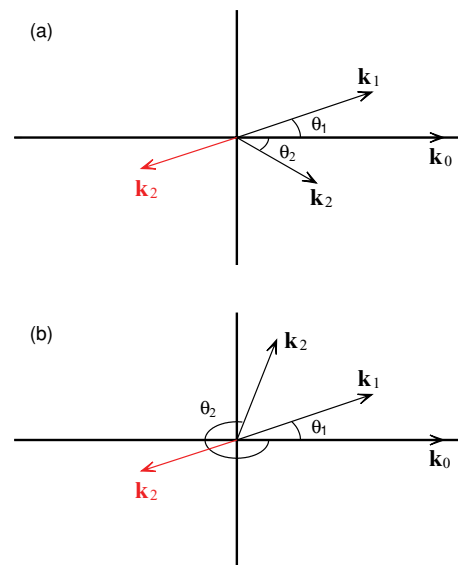FIG. 10. (Color online) Geometry of momentum vectors for the corresponding laser-free $(e,2e)$ processes in Figs. 8 and 9.

ejected electron energy increases. This is because for fixed $k_1^\perp$ the ejected electron obtains the same amount of $-k_2^\perp$ at a smaller outgoing angle with larger energy. In contrast, the P-CCC predicts a much lower binary peak due to the Coulomb repulsion between the two electrons. As shown in Fig. 10(a), when the ejected electron appears at the position where a strong binary peak is produced in the P-CC model, the two electrons are close to each other such that k_{12} is small and consequently α_{12} in Eq. (9) is large. In this situation, a very strong Coulomb force acts on the two electrons and prevents them from approaching each other. This strong Coulomb interaction forces the ejected electron to move along the opposite direction of the projectile, as illustrated in Fig. 10 by the left (red) arrow, such that a high backward peak in the TDCS is predicted by the P-CCC model around $\theta_2 = 180°$ (see the dotted line in Fig. 9). The P-CC model also reproduces a high peak around $\theta_2 = 310°$, which corresponds to the geometry displayed in Fig. 10(b). In this case, the two electrons are close to each other again. For the same reason, the P-CCC predicts almost zero cross section for $\theta_2 > 270°$. For smaller scattering angle θ_1, generally a larger TDCS is expected. However, the binary collision is suppressed significantly by the Coulomb interaction.

It should be noted that for higher incident energy, k_{12} increases and the Coulomb interaction becomes weaker when the ejected electron goes out in the direction when $k_2^\perp = -k_1^\perp$. Consequently, a relatively stronger binary peak can be generated in the P-CCC model.

B. Correlated electron spectra due to excitation-ionization processes in strong laser fields

In Sec. II E, we separated the $(e,2e)$ and the tunneling-excitation spectra from the total experimental measurements, as shown in Fig. 4. Before presenting the details of our simulation procedures for the excitation-tunneling process, we first show the calculated final volume integrated tunneling-excitation spectra in Fig. 11(a). This is to be compared to the corresponding experimental data in Fig. 11(b), which are taken from Fig. 4(c). Significant discrepancies are found between the two. The experimental data show distributions, called the "cross," along the axes $p_1^\parallel = 0$ and $p_2^\parallel = 0$, which are absent in the theoretical simulation. In fact, according to the kinematical analysis, as shown in Fig. 3, the cross appears in the kinematically forbidden region. Therefore, if the cross is real, then it must be attributed to some other mechanisms. This is addressed later.

Using the electron-momentum spectra calculated from the excitation-tunneling mechanism, shown in Fig. 11(a), we separate out the experimental spectra in Fig. 11(b) into the sum of Fig. 11(c) and Fig. 11(d); the former is the correlation spectra from the new mechanism which we have not yet addressed, and the latter is the correlation spectra from the true excitation tunneling. In other words, the theoretical simulation for excitation tunneling should be compared to the experimental data in Fig. 11(d), instead of Fig. 11(b). This separation is done by assuming that the sum spectra in the four corners of Fig. 11(b) are all due to true excitation-tunneling process. By multiplying the theoretical spectra by a constant and adjusting it until the spectra in the four corners in Fig. 11(b)
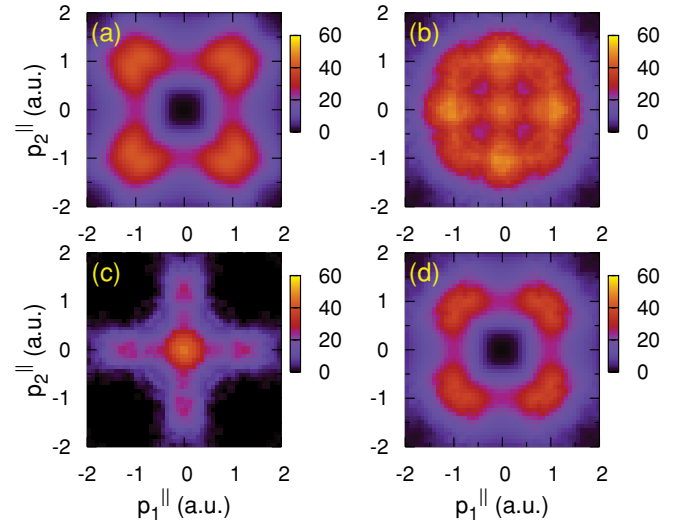

FIG. 11. (Color online) Correlated parallel momentum spectra for NSDI of He in a laser pulse with wavelength of 800 nm at peak intensity of 4.5×10^{14} W/cm^2. (a) Theoretical simulations for excitation tunneling only. (b) Experimental spectra with the $(e,2e)$ part subtracted. It contains excitation-tunneling process plus other possible mechanisms. (c) Deduced correlated electron spectra from experiment that are attributed to new mechanisms, that is, the remaining experimental spectra after the $(e,2e)$ and excitation-tunneling parts have been subtracted. (d) Deduced true experimental correlated electron spectra from the excitation-tunneling process. See the text for details.

have the best fit, we then attribute the remaining part to be the cross." Once the cross is obtained, we obtain Fig. 11(d) to be the difference between Fig. 11(b) and Fig. 11(c). Any negative values are replaced by zeros in the substraction process.

To generate correlated momentum spectra for excitation tunneling in a strong laser field, we first calculate the singlet DCS for laser-free electron-impact excitation. In our calculations, Coulomb waves are used to describe the projectile electron, for both the initial and the final states. In Fig. 12, the DCS for excitations of He$^+$ from the ground state to $2s$, $2p$,
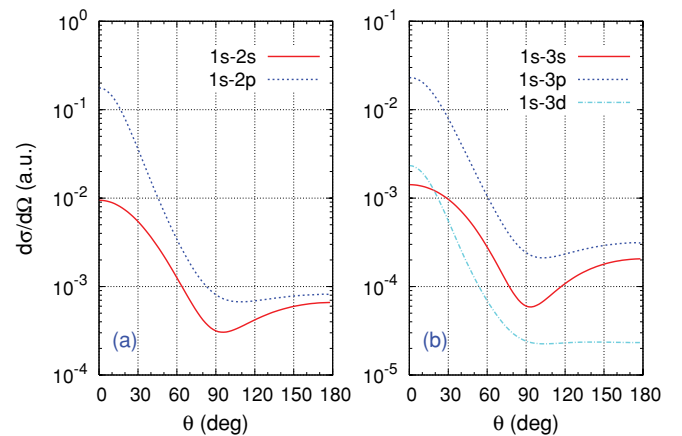

FIG. 12. (Color online) (Differential cross sections for laser-free electron-impact excitation of He$^+$ from $1s$ state to the excited states of (a) $n = 2$ and (b) $n = 3$. The incident energy is 85 eV. The total spin of the two electrons is restricted to $S = 0$.
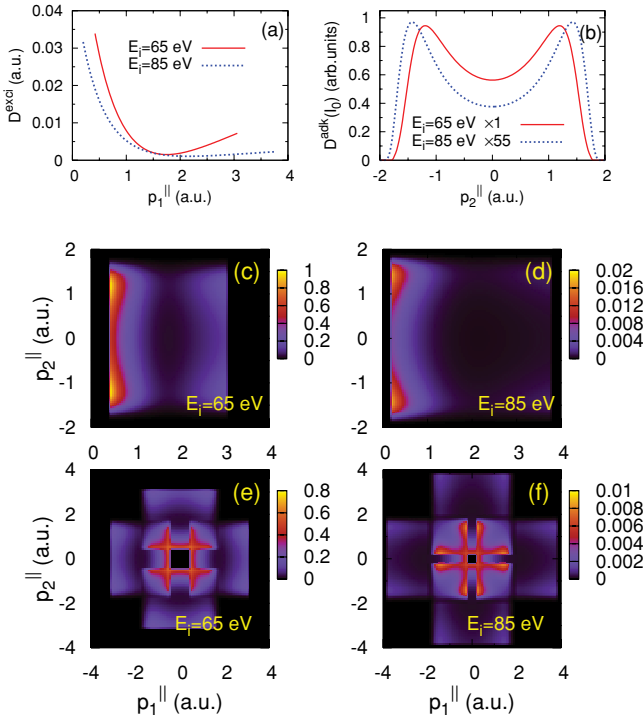
FIG. 13. (Color online) (a) Parallel momentum spectra for the recollision electron after colliding with He$^+$ ion and exciting the $1s$ ground state electron to the $2s$ state at energies of 65 and 85 eV. The recollision electron is returning along $-\hat{z}$ direction. (b) Volume-integrated parallel momentum spectra for an electron ionized from He$^+$ ($2s$) by a 45-fs laser pulse with wavelength of 800 nm at the peak intensity of 4.5×10^{14} W/cm^2. (c) Right side ($p_1^{\|} > 0$) correlated parallel momentum spectra for excitation tunneling in strong-field NSDI for a returning electron with an energy of 65 eV along $-\hat{z}$ direction. (d) Same as (c) but for returning electron energy of 85 eV. (e) Symmetrized correlated parallel momentum spectra from the spectra in (c). (f) Symmetrized correlated parallel momentum spectra from the spectra in (d).

$3s$, $3p$, and $3d$ states as function of scattering angles for an incident energy of 85 eV are shown. The DCS drops rapidly as the scattering angle increases. Furthermore, excitation to the $n = 3$ states are about one order of magnitude smaller. Thus excitations to higher n states are not considered.

From the laser-free DCS, we can readily obtain parallel photoelectron momentum spectra for a given recollision energy by using Eqs. (37) and (38). For electrons returning along the $-\hat{z}$ direction with energies of 65 and 85 eV, for excitation of He$^+$ from the $1s$ to $2s$ state, their parallel momentum spectra are shown in Fig. 13(a). Note that the momentum shift by the vector potential at the time of recollision has been included. Thus, for example, for the 85-eV incident electron, the parallel photoelectron momentum covers the range of 0.2 to 3.8 a.u. A narrower parallel momentum range is covered if the incident energy is 65 eV, as seen in Fig. 13(a).

We next calculate the tunneling ionization rate from the excited states and their corresponding parallel momentum distributions. Consider the parallel momentum spectra for an electron in the $2s$ excited state in an 800-nm laser, with pulse duration of 45 fs and peak intensity of 4.5×10^{14} W/cm^2. In

Fig. 13(b), we plot the focal volume integrated results obtained from Eq. (46) corresponding to incident energies of 65 and 85 eV. Both show double-hump structures with a minimum at the center around $p_2^{\|} = 0$ within $(-A_0, A_0)$, where $A_0 = 2.0$ is the maximum value of the vector potential. It should be noted that the volume-averaged $p_2^{\|}$ spectra are different for $E_i = 65$ and 85 eV. Although they have similar shape, the magnitude for 85 eV is about 55 times smaller. This is because the focal volume which can generate 65-eV returning electrons is much larger than the one which can generate 85-eV electrons. Since electrons in the excited states are readily ionized, the calculated momentum spectra is very sensitive to the laser intensity. In general, at lower intensity, the momentum spectra has higher distribution at the center. As the intensity increases, the distribution at the center is depressed. To understand this, recall that excitation occurs when the electric field of the laser is near zero or when the vector potential is near the peak. As the electric field $E(t)$ increases at time t, tunneling ionization occurs and the electron emerges with a momentum given by the vector potential $A(t)$. For high intensities, electrons are quickly ionized such that the ionization rate is small, due to depletion, when the electric field reaches its maximum value, where $A(t)$ is close to zero. From this discussion, it is clear that the momentum spectra for an electron tunnel ionized from higher excited states (for n greater than 2) will have very small or even zero distribution at the center since it is ionized immediately after excited by the returning electron.

The correlated momentum spectra is a product of parallel momentum distribution of the recollision electron after excitation, as shown in Fig. 13(a), and the momentum yield of the excited electron after tunnel ionization, as shown in Fig. 13(b) [see Eq. (45)]. Figures 13(c) and 13(d) show the two-dimensional correlated momentum spectra for a returning (incident) electron with energies of 65 and 85 eV, respectively, for the electron excited to the $2s$ state.

The distributions in Figs. 13(c) and 13(d) form the basis for understanding the correlated electron distributions from the excitation-tunneling ionization process of NSDI. For the distributions in $p_1^{\|}$ [i.e., the momentum of the recolliding (incident) electron], the kinematic constraint in Fig. 3 says that the lower limit of $p_1^{\|}$ moves away from $p_1^{\|} = 0$ as the returning electron energy decreases. The $p_1^{\|}$ distributions are determined by the differential excitation cross sections—see Fig. 13(a)—where scattering to large angles is much less likely. This makes the actual width in the $p_1^{\|}$ distribution much narrower than the range shown in Fig. 3, which considers the kinematics only. For the distribution in $p_2^{\|}$, it is determined by the vector potential at the time of tunneling ionization of the excited electron.

The distributions in Figs. 13(c) and 13(d) are for electrons returning along $-\hat{z}$. Based on the symmetry shown in Fig. 3, we can obtain the total correlated electron-momentum spectra for the excitation-tunneling processes shown in Figs. 13(e) and 13(f).

The final correlated momentum spectra for the two outgoing electrons in the excitation-tunneling process is obtained by means of Eq. (47) to account for the energy distribution of the returning electrons. The result for the $2s$ state is shown in Fig. 14(a).
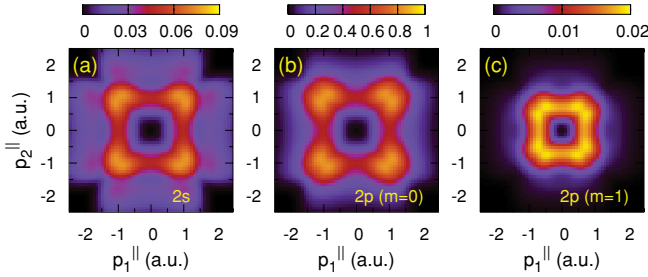
FIG. 14. (Color online) Theoretical correlated parallel momentum spectra for excitation tunneling in a laser pulse with wavelength of 800 nm at peak intensity of 4.5×10^{14} W/cm^2. The electron that is excited and then tunnel ionized is in the states (a) He$^+$ (2s), (b) He$^+$ (2p) ($m = 0$), and (c) He$^+$ (2p) ($m = 1$), respectively.

To account for all the excited states that are populated by the returning electrons, we also perform similar calculations for the $2p$, $3s$, $3p$, and $3d$ excited states. Note that for $l > 0$, the calculations are carried out for each magnetic quantum number m, except that the yield for m and $-m$ states are identical. The correlated electron-momentum spectra, after including the volume integration, for the $2p$ state with $m = 0$ and $m = 1$ are shown in Figs. 14(b) and 14(c), respectively. Note that for a given n, the contribution from the np state is the largest. They are the so-called optical allowed transitions; that is, they can be reached by absorbing one single photon from the $1s$ state of He$^+$. Within the np substates, the $m = 0$ is larger than $m = \pm 1$, since the excitation DCS decreases when $|m|$ increases. In addition, tunneling ionization favors the $m = 0$ states, which implies that the momentum distribution of tunneling ionization is enhanced at small momenta for large $|m|$. This explains why the correlated momentum spectrum in Fig. 14(c) for $m = 1$ shrinks compared with that in Fig. 14(b) for $m = 0$. The sum of the correlation spectra from all the $n = 2$ and $n = 3$ excited states has already been shown in Fig. 11(a).

C. Capture-tunneling ionization as a new mechanism for NSDI

According to our analysis of the correlation spectra in NSDI so far, we are left with the spectra in Fig. 11(c), which cannot be attributed to either the (e,$2e$) or the excitation-tunneling processes. We suggest that this distribution is due to the capture-tunneling mechanism in which the returning electron is captured by dielectronic recombination with He$^+$ (1s) ion to form a doubly excited state, say, the He ($2s2p$) state. In field-free situations, this is a resonance process, and the doubly excited state can be stabilized by emitting a photon or by autoionization. In the laser field, the two electrons in the doubly excited states are easily tunnel ionized, thus contributing to the NSDI events. Since dielectronic recombination is a resonant process, for He ($2s2p^1P$), the returning electron must have the fixed energy of 35.6 eV. The lowest single peak intensity of the laser field capable of generating this electron energy is 1.9×10^{14} W/cm^2. Since doubly excited states are highly correlated, we cannot say which electron will tunnel out first. For the qualitative discussion here, we say that it is the $2p$ electron that is ionized first. Since the binding energy of He ($2s2p$) is only 5.2 eV (with respect to the $2s$ or $2p$ states of
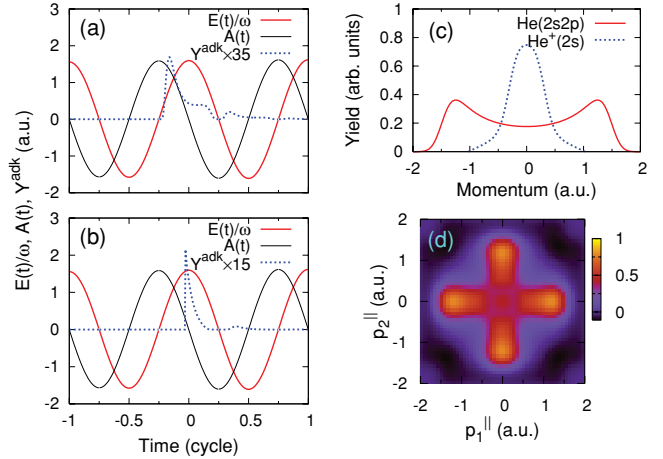

FIG. 15. (Color online) (a) Ionization of He ($2s2p$) vs time in a laser with wavelength of 800 nm at peak intensity of 3.0×10^{14} W/cm^2. The electric field and vector potential of the laser in a cycle are also indicated. (b) Same as (a) but for He$^+$(2s); (c) parallel momentum distribution for electrons tunnel ionized from He ($2s2p$) and He$^+$ (2s), respectively; (d) and correlated parallel momentum spectra generated from momentum distributions in (c).

He$^+$), the first electron will be tunnel ionized soon after its formation, that is, at the time when the laser's electric field is small or when the vector potential is large. This process will produce the first continuum electron with large drift velocity near the maximum of the vector potential. Choosing a laser field with the single peak intensity of 3.0×10^{14} W/cm^2 as an example, we show the ionization rate as a function of time together with the electric field and the vector potential in Fig. 15(a). It can be seen in Fig. 15(a) that the $2p$ electron in He ($2s2p$) is almost completely ionized before the electric field reaches its maximum value. As a result, the ionization of the $2s$ electron in He$^+$ (2s) gets started soon after. However, the ionization potential of He$^+$(2s) is 13.6 eV; it is tunnel ionized near the peak of the electric field only and thus emerges with a near-zero drift momentum. The ionization rate as a function of time for the tunneling of the He$^+$ (2s) electron is plotted in Fig. 15(b). The corresponding momentum distributions for these two tunneling processes are shown in Fig. 15(c). The correlated momentum spectra can be constructed by taking the product of the momentum distributions of the tunneling processes of the two electrons, as shown in Fig. 15(d). Clearly the calculations can be applied to other doubly excited states like $2s2s(^1S)$ and $2p2p$ ($^1S,^1D$) formed by the rescattering process. We assume that they all have the same shape. Note that we need to include singlet doubly excited states only as the total spin is conserved for the two-electron system. In this analysis, we do not include doubly excited states where one of the electrons has a principal quantum number greater than 2. They would contribute more to the four corners of the cross in Fig. 15(d), but their contributions are expected to be small.

A comparison of the simulated correlation spectra in Fig. 15(d) with the cross in Fig. 11(c) shows that capture tunneling does not reproduce the central peak of the cross at the origin. To isolate an additional possible mechanism, we use the same procedure used in Fig. 11 to obtain Fig. 16. Here we assume that the outer portions of the cross are due
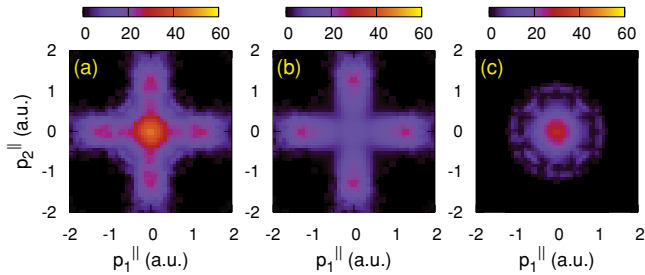
FIG. 16. (Color online) Deduced experimental correlated parallel momentum spectra. (a) The remaining spectra after the (e,2e) and excitation-tunneling part are excluded. (b) Capture-tunneling part only. (c) The remaining part in (a) excluding the capture-tunneling portion. This part is attributed to multiphoton double ionization or single ionization followed by a shakeoff process.

to capture tunneling. The remaining distributions near the origin are shown in Fig. 16(c). Since both electrons have small momenta, any processes that produce two low-energy electrons should be considered. They can include multiphoton double ionization (MPDI), or single ionization followed by the shakeoff of the second electron, for helium from the ground state. Photoionization of doubly excited states is not considered to be likely since they would be ionized at lower electric fields of the laser and emerge with higher momenta for both electrons. At this moment, we do not have an efficient simple model to estimate these contributions.

D. Recoil-ion longitudinal momentum distributions

From the correlated two-electron longitudinal momentum spectra, we obtain the longitudinal momentum spectra of He^{2+} ions, shown in Fig. 17. Recall that we first separate the
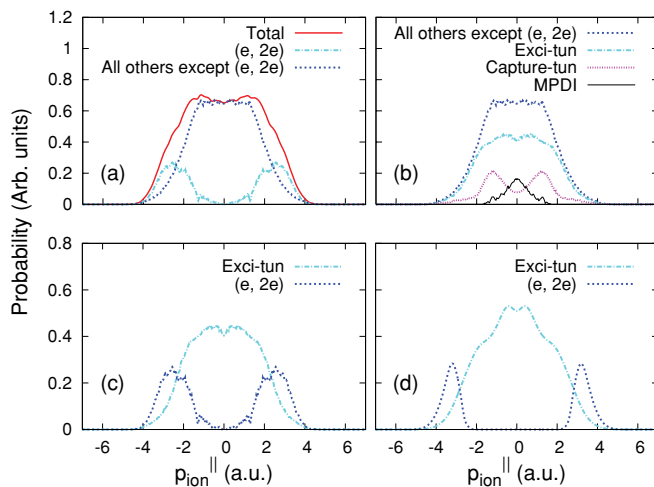

FIG. 17. (Color online) Longitudinal momentum distribution of He^{2+} ions for NSDI of He in a laser pulse with wavelength of 800 nm at peak intensity of 4.5×10^{14} W/cm². (a) Separation of the total experimental spectra into (e,2e) and all other mechanisms; (b) separation of the experimental spectra of all mechanisms except (e,2e) into excitation tunneling, capture tunneling, and multiphoton double ionization; (c) experimental spectra of excitation tunneling and (e,2e); and (d) theoretical spectra of excitation tunneling and (e,2e).

correlated momentum distributions of the experimental data into two parts: one is (e,2e) and the other is mainly excitation tunneling, as shown in Fig. 4. In Fig. 17(a), the experimental momentum spectra of He^{2+} ion are separated into the (e,2e) part and the non-(e,2e) part. From the result, we calculated that the (e,2e) part contributes only a small portion (about 24%) to the total NSDI.

Following the analysis in Sec. III C, we also calculated the He^{2+} ion momentum distributions from the experimental correlated momentum spectra, for the true tunneling ionization, capture-tunneling, and MPDI mechanisms, respectively, and the results are plotted in Fig. 17(b). From these distributions, we calculated that the three non-(e,2e) processes make contributions of 53%, 17%, and 6%, respectively, totaling 76% of the NSDI.

We have not evaluated the ion-momentum distributions theoretically for capture-tunneling or MPDI mechanisms so far. Thus we compare ion-momentum distributions in Figs. 17(c) and 17(d) for the true excitation-tunneling process and the (e,2e) process, from the calculation versus from the experiment. For the (e,2e) part, the results are from the DS3C model. From the comparison in Figs. 17(c) and 17(d), one can see that while the main features of the ion-momentum distributions in the experimental data are well reproduced by theoretical simulations, the theoretical distributions for the (e,2e) part on each side in Fig. 17(d) are somewhat narrower than the experimental one. This is the consequence of the wider angle between the two recoil peaks in Fig. 7(c) as compared to the experimental data seen in Fig. 7(d)—a consequence of too much electron-electron repulsion included in the DS3C model. For excitation tunneling, the distribution near the top is much flatter from the experiment than from theory. Despite this, the main features of ion-momentum distribution are well reproduced in the simulation.

IV. SUMMARY AND FUTURE DIRECTIONS

In this paper, we applied the recently developed QRS theory to the nonsequential double ionization of a helium atom in an intense laser field. According to the rescattering model, double ionization may occur via direct (e,2e)-type ionization of the target ion or by collisional excitation of the parent ion followed by tunnel ionization. Using the QRS model and standard field-free electron-scattering theories to evaluate the correlated two-electron longitudinal momentum spectra reported by Staudte et al. [15], we draw the following major conclusions: (1) Tunneling ionization is the dominant NSDI mechanism for the experiment of Staudte et al. (2) The fingerlike structure observed in the experiment is due to the (e,2e) collisions, and the structure can be explained only when the effect of electron-electron repulsion is included in the final state. (3) Based on the kinematic analysis, there are features in the correlated electron spectra that cannot be explained by the (e,2e) or the excitation-tunneling mechanisms. We suggest that a big portion of the remaining features be attributed to capture-tunneling ionization where the returning electron is captured by the ion to form doubly excited states. The two excited electrons are then sequentially tunnel ionized by the laser field. (4) The experimental data also showed pronounced double-ionization yields where both electrons have small

momenta. We suggested that they may arise from double ionization by multiphoton absorption or single ionization followed by shake-off process—from the ground state. The mechanisms suggested in (3) and (4) account for only a small portion of the total double-ionization events, but their presence is quite noticeable in the correlated electron spectra.

There remains much to be investigated for the NSDI processes. Experimentally it would be desirable to study NSDI at the level of momentum distributions of both electrons, using lasers of longer or shorter wavelengths and at different intensities. Since the relative importance of the interaction between two electrons depends on the energies of the returning electrons, these studies can shed new light on the models used for electron-impact excitation and ionization of atomic ions. Such studies can bridge strong-field physics with the conventional electron-collision physics. On the theory side,

built on the present work, more sophisticated field-free collision theories can be employed within the QRS model to obtain more accurate quantitative results. Clearly a push for such better calculations would become desirable only if a more extended set of correlated electron spectra over a range of laser parameters is available.

[1] P. B. Corkum, Phys. Rev. Lett. **71**, 1994 (1993).

[2] J. L. Krause, K. J. Schafer, and K. C. Kulander, Phys. Rev. Lett. **68**, 3535 (1992).

[3] D. N. Fittinghoff, P. R. Bolton, B. Chang, and K. C. Kulander, Phys. Rev. Lett. **69**, 2642 (1992).

[4] T. Auguste, P. Monot, L. A. Lompré, G. Mainfray, and C. Manus, J. Phys. B **25**, 4181 (1992).

[5] B. Walker, B. Sheehy, L. F. DiMauro, P. Agostini, K. J. Schafer, and K. C. Kulander, Phys. Rev. Lett. **73**, 1227 (1994).

[6] B. Sheehy, R. Lafon, M. Widmer, B. Walker, L. F. DiMauro, P. A. Agostini, and K. C. Kulander, Phys. Rev. A **58**, 3942 (1998).

[7] A. Talebpour, S. Larochelle, and S. L. Chin, J. Phys. B **30**, L245 (1997).

[8] C. Cornaggia and Ph. Hering, J. Phys. B **31**, L503 (1998).

[9] C. Guo, M. Li, J. P. Nibarger, and G. N. Gibson, Phys. Rev. A **58**, R4271 (1998).

[10] Th. Weber, H. Giessen, M. Weckenbrock, G. Urbasch, A. Staudte, L. Spielberger, O. Jagutzki, V. Mergel, M. Vollmer, and R. Dörner, Nature (London) **405**, 658 (2000).

[11] B. Feuerstein *et al.*, Phys. Rev. Lett. **87**, 043003 (2001).

[12] E. Eremina *et al.*, J. Phys. B **36**, 3269 (2003).

[13] R. Moshammer *et al.*, J. Phys. B **36**, L113 (2003).

[14] M. Weckenbrock *et al.*, Phys. Rev. Lett. **92**, 213002 (2004).

[15] A. Staudte *et al.*, Phys. Rev. Lett. **99**, 263002 (2007).

[16] A. Rudenko, V. L. B. de Jesus, Th. Ergler, K. Zrost, B. Feuerstein, C. D. Schröter, R. Moshammer, and J. Ullrich, Phys. Rev. Lett. **99**, 263003 (2007).

[17] Y. Liu, S. Tschuch, A. Rudenko, M. Dürr, M. Siegel, U. Morgner, R. Moshammer, and J. Ullrich, Phys. Rev. Lett. **101**, 053001 (2008).

[18] S. L. Haan, Z. S. Smith, K. N. Shomsky, and P. W. Plantinga, J. Phys. B **42**, 134009 (2009).

[19] M. Lein, E. K. U. Gross, and V. Engel, Phys. Rev. Lett. **85**, 4707 (2000).

[20] C. Ruiz, L. Plaja, L. Roso, and A. Becker, Phys. Rev. Lett. **96**, 053001 (2006).

[21] J. S. Prauzner-Bechcicki, K. Sacha, B. Eckhardt, and J. Zakrzewski, Phys. Rev. Lett. **98**, 203002 (2007).

[22] J. S. Parker, B. J. S. Doherty, K. T. Taylor, K. D. Schultz, C. I. Blaga, and L. F. DiMauro, Phys. Rev. Lett. **96**, 133001 (2006).

[23] A. Becker and F. H. M. Faisal, Phys. Rev. Lett. **89**, 193003 (2002).

[24] C. Figueira de Morisson Faria, H. Schomerus, X. Liu, and W. Becker, Phys. Rev. A **69**, 043405 (2004).

[25] C. Figueira de Morisson Faria, X. Liu, and W. Becker, Phys. Rev. A **69**, 021402(R) (2004).

[26] A. Becker and F. H. M. Faisal, J. Phys. B **38**, R1 (2005).

[27] T. Shaaran, M. T. Nygren, and C. Figueirade Morisson Faria, Phys. Rev. A **81**, 063413 (2010).

[28] D. F. Ye, X. Liu, and J. Liu, Phys. Rev. Lett. **101**, 233003 (2008).

[29] A. Emmanouilidou, Phys. Rev. A **78**, 023411 (2008).

[30] Z. Chen, A.-T. Le, T. Morishita, and C. D. Lin, Phys. Rev. A **79**, 033409 (2009).

[31] A.-T. Le, T. Morishita, and C. D. Lin, Phys. Rev. A **78**, 023814 (2008).

[32] A.-T. Le, R. R. Lucchese, S. Tonzani, T. Morishita, and C. D. Lin, Phys. Rev. A **80**, 013401 (2009).

[33] C. D. Lin, A.-T. Le, Z. Chen, T. Morishita, and R. Lucchese, J. Phys. B **43**, 122001 (2010).

[34] S. Micheau, Z. Chen, A.-T. Le, and C. D. Lin, Phys. Rev. A **79**, 013417 (2009).

[35] M. Brauner, J. S. Briggs, and H. Klar, J. Phys. B **22**, 2265 (1989).

[36] M. Brauner, J. S. Briggs, H. Klar, J. T. Broad, T. Rosel, K. Jung, and H. Ehrhardt, J. Phys. B **24**, 657 (1991).

[37] J. Berakdar and J. S. Briggs, Phys. Rev. Lett. **72**, 3799 (1994).

[38] Z. Chen, Q. Shi, S. Zhang, J. Chen, and K. Xu, Phys. Rev. A **56**, R2514 (1997).

[39] Z. Chen, Y. Liang, and C. D. Lin, Phys. Rev. Lett. **104**, 253201 (2010).

[40] G. L. Yudin and M. Yu. Ivanov, Phys. Rev. A **64**, 035401 (2001).

[41] S. Augst, D. D. Meyerhofer, D. Strickland, and S. L. Chin, J. Opt. Soc. Am. B **8**, 858 (1991).

[42] M. V. Ammosov, N. B. Delone, and V. P. Krainov, Zh. Eksp. Teor. Fiz. **91**, 2008 (1986) [Sov. Phys. JETP **64**, 1191 (1986)].

[43] X. M. Tong and C. D. Lin, J. Phys. B **38**, 2593 (2005).

[44] X. M. Tong, Z. X. Zhao, and C. D. Lin, Phys. Rev. A **66**, 033402 (2002).